

GT2015-43298

## COMPARISON OF THE THREE-DIMENSIONAL BOUNDARY LAYER ON FLAT VERSUS CONTOURED TURBINE ENDWALLS

Stephen P. Lynch

Karen A. Thole

Mechanical and Nuclear Engineering Department

The Pennsylvania State University

University Park, PA 16802, USA

### ABSTRACT

The boundary layer on the endwall of an axial turbomachine passage is influenced by streamwise and cross-stream pressure gradients, as well as a large streamwise vortex, that develop in the passage. These influences distort the structure of the boundary layer and result in heat transfer and friction coefficients that differ significantly from simple two-dimensional boundary layers. Three-dimensional contouring of the endwall has been shown to reduce the strength of the large passage vortex and reduce endwall heat transfer, but the mechanisms of the reductions on the structure of the endwall boundary layer are not well understood.

This study describes three-component measurements of mean and fluctuating velocities in the passage of a turbine blade obtained with a laser Doppler velocimeter. Friction coefficients obtained with the oil film interferometry method were compared to measured heat transfer coefficients. In the passage, the strength of the large passage vortex was reduced with contouring. Regions where heat transfer was increased by endwall contouring corresponded to elevated turbulence levels compared to the flat endwall, but the variation in boundary layer skew across the passage was reduced with contouring.

### INTRODUCTION

Three-dimensional boundary layers are found in many practical situations where a cross-stream pressure gradient exists to turn the flow, such as in curved channels, around the base of bridge piers, and at the endwall of axial turbomachine passages. Through a simple Euler analysis, it can be shown that the lower velocity of the wall boundary layer relative to the freestream results in a smaller radius of curvature than the freestream, when both are subjected to the same cross-stream pressure gradient. Skew between the freestream and near-wall flow direction develops, and the structure of the turbulence is distorted when compared to a simpler two-dimensional boundary layer.

The presence of a velocity component in the cross-stream direction implies mean streamwise vorticity in a three-dimensional boundary layer. In an axial turbine, additional streamwise vorticity is generated when the inlet boundary layer separates upstream of the airfoil leading edge and is convected around the airfoil. Previous studies (Langston, et al. [1], Sharma and Butler [2], Sieverding [3], and others) have indicated that these two sources of streamwise vorticity merge to create a large streamwise vortex, also known as a passage vortex. This vortex is a significant source of aerodynamic loss and locally increases endwall heat transfer. However, the effects of the passage vortex on the characteristics of the three-dimensional boundary layer have not been presented, likely due to the difficulty in measuring the endwall boundary layer in a blade passage.

To mitigate the detrimental effects of the passage vortex, three-dimensional contouring of the endwall surface has been studied. Elevations and depressions in the endwall shape locally decrease or increase the static pressure, respectively, to limit or distort the formation of the passage vortex. Generally the freestream flow remains the same; only the endwall flow is affected. It has also been shown that the contouring can reduce endwall heat transfer, although the connection between the endwall boundary layer and the surface heat transfer is not yet understood.

The objective of this study was to perform a detailed examination of a three-dimensional boundary layer influenced by a large streamwise vortex. The application of endwall contouring provided a means of modifying the streamwise vortex to gauge its influence on the endwall boundary layer, surface heat transfer, and wall friction coefficients. The experimental data set given here will provide useful information to improve physical models.

### NOMENCLATURE

BL        boundary layer  
 $C_{ax}$      axial chord of blade

$C_f$	friction coefficient, $C_f = \frac{\tau_w}{1/2\rho U_{edge}^2}$
$C_p$	constant-pressure specific heat
$D$	diameter of LDV measurement volume
$h$	heat transfer coefficient, $h = q_w'' / (T_w - T_{in})$
$H$	boundary layer shape factor, $H = \delta^* / \theta$
HS	horseshoe vortex
$k$	turbulent kinetic energy (TKE), $k = \frac{1}{2}(\overline{u'^2} + \overline{v'^2} + \overline{w'^2})$
$L$	length of LDV measurement volume
OFI	oil film interferometry
$P$	blade pitch
$Pr$	Prandtl number
PS	pressure side
$q_w''$	wall heat flux
$Re_s$	streamwise Reynolds number, $Re_s = sU_{edge} / \nu$
$Re_\theta$	momentum thickness Reynolds no., $Re_\theta = \theta U_{edge} / \nu$
$s$	limiting streamline direction
$S$	blade span
SS	suction side
$St$	Stanton number, $St = h / \rho C_p U_{edge}$
$T$	temperature
$x, y, z$	local coordinates; see Figure 2
$X, Y, Z$	cascade coordinates, where $X$ is blade axial direction
$u, v, w$	velocity components in a local coordinate system
$U, V, W$	velocity components in the cascade coordinate system
$V_s, V_n, V_z$	secondary velocity components; Eq.'s (2-4)
$u_\tau$	friction velocity, $u_\tau = \sqrt{\tau_w / \rho}$
$U_{in}$	magnitude of inlet streamwise velocity
$U_{exit}$	magnitude of exit streamwise velocity
$U_{edge}$	magnitude of local freestream velocity at the BL edge

### **Greek**

$\beta$	mean flow angle
$\delta_{99}$	boundary layer thickness (99%)
$\delta^*$	displacement thickness based on streamwise velocity, $\delta^* = \int_0^\infty \left(1 - \frac{u}{U_{edge}}\right) dz$
$\theta$	momentum thickness based on streamwise velocity, $\theta = \int_0^\infty \frac{u}{U_{edge}} \left(1 - \frac{u}{U_{edge}}\right) dz$
$\mu$	dynamic viscosity
$\nu$	kinematic viscosity
$\rho$	density
$\tau_w$	wall shear stress

### **Subscripts**

edge	quantity at boundary layer edge
exit	exit freestream conditions
in	inlet freestream conditions
ms	midspan (inviscid) conditions
w	wall conditions

### **Superscripts**

'	fluctuating quantity
$(\bar{\quad})$	time-averaged quantity

### **RELEVANT PAST STUDIES**

Flow near the endwall of an axial turbine is extremely complicated due to the interaction of cross-stream and streamwise pressure gradients, separation and reattachment of the endwall boundary layer, large vortical structures, high freestream turbulence, upstream airfoil wakes, transitional flow, compressibility effects, and so on. Despite a body of work addressing these effects on endwall flow, very few studies have examined the three-dimensional endwall boundary layer in detail. A three-dimensional boundary layer is termed as such due to the presence of a cross-flow velocity component (normal to the streamwise direction).

Fundamental characteristics of three-dimensional turbulent boundary layers have been examined for wedge-type flows with relatively low flow turning. Anderson and Eaton [4] determined that the Reynolds shear stress lagged the strain rate in a three-dimensional boundary layer generated by a wedge in the flow, resulting in anisotropic eddy viscosity. Also, the ratio of the magnitude of the shear stress to the turbulent kinetic energy was lower for the three-dimensional boundary layer in comparison to two-dimensional boundary layers, implying reduced effectiveness of the boundary layer at generating Reynolds shear stresses. A review of several three-dimensional boundary layer data sets by Johnston and Flack [5] showed that the ratio of the shear stress magnitude to the turbulent kinetic energy tended to decrease as the total skew angle between the freestream and the wall shear increased. Measurements by Lewis and Simpson [6] around a wing-body junction indicated that time-mean heat transfer decreased relative to a two-dimensional flat plate correlation for increasing boundary layer three-dimensionality. The combined effects of a streamwise vortex and a pressure-driven three-dimensional boundary layer were considered by Shizawa and Eaton [7]. A streamwise vortex with near-wall induced velocity in the same direction as the crossflow reduced the strength of ejection events linked to turbulent stresses. Based on the above, it would seem that high levels of skew are beneficial.

It is not entirely clear, however, what the state of the endwall boundary layer is within a turbine passage. Single component hot-wire measurements in the cascade of Langston, et al. [1] indicated a very thin, possibly laminar boundary layer on the endwall downstream of the inlet boundary layer separation. Harrison [8] found that the momentum Reynolds number was less than  $Re_\theta=200$  over a large part of the endwall downstream of the horseshoe vortex separation. Hot-film signals in that region also exhibited much lower RMS values as compared to the upstream turbulent boundary layer. Hot film signals presented by Vera, et al. [9] indicated low amplitudes near the pressure side, suggesting laminar-like flow.

One method of mitigating detrimental effects of secondary flows in a turbine is three-dimensional (also termed non-axisymmetric) contouring of the endwall, where local curvature is generated to reduce cross-passage pressure gradients. Harvey, et al. [10] was among the first to discuss a computational optimization of the endwall intended to minimize exit flow angle deviations and pitchwise static pressure gradients. Experimental validation by Hartland, et al. [11] found a 30% reduction in aerodynamic losses for the contoured wall relative to a flat wall. Endwall contouring in the studies of Germain, et al. [12] and Schuepbach, et al. [13] produced an overall stage efficiency improvement of  $1.0\% \pm 0.4\%$  in a 1-1/2 stage turbine, which was largely attributed to reductions in the stator time-averaged and unsteady losses. Praisner, et al. [14] designed a non-axisymmetric endwall contour based on secondary loss reduction metrics for the airfoil in this study. The endwall contour reduced losses (4% predicted, 10% measured) and turbulent kinetic energy levels associated with the secondary flow, when compared to the flat endwall. Experiments on the same geometry by Knezevici, et al. [15] showed a reduction in passage vortex strength with the contour, although the corner vortex and near-wall passage crossflow were intensified near the trailing edge where the contour merged back to the flat endwall level.

Recent studies of endwall heat transfer with contouring suggest that it is favorably reduced by changes to the passage vortex. Saha and Acharya [16] computationally evaluated nine endwall shapes and found that the best design reduced overall heat transfer by 8%, with significant reductions of over 300% near the suction side leading edge and approximately 20% in the throat compared to a flat endwall. Panchal, et al. [17] also found reductions in local and endwall-average heat transfer at high subsonic conditions for contoured endwalls, attributed to redirection of the passage vortex with contouring. A contour studied by Lynch, et al. [18] (same as in this study) significantly decreased endwall heat transfer near the pressure side of the passage relative to a flat endwall, which was attributed to reduced strength of the passage vortex. Although CFD predictions of the flat endwall heat transfer by Lynch, et al. [19] did not agree with the measurements of Lynch, et al. [18], trends of heat transfer augmentation due to contouring were reasonably captured.

The study presented in this paper is unique in several aspects. First, the large amount of skew present in the turbine blade passage exceeds the current level of skew that has been measured for three-dimensional boundary layers in the literature. Furthermore, there have been few measurements of the three-dimensional mean and turbulent flowfield in the forward region of a blade passage, where the passage vortex originates. Finally, there have been no direct measurements of the endwall boundary layer within a turbine cascade, particularly with the application of non-axisymmetric endwall contouring.

## EXPERIMENTAL METHODOLOGY

A large scale turbine blade cascade was placed in a closed loop wind tunnel for this study, as shown in Figure 1a. The operation of the tunnel, as well as the cascade design and benchmarking, have been described previously by Lynch, et al. [18]. A turbulence grid with a bar width of 2.54 cm and 10.2 cm spacing between bar centers was placed approximately 11 axial chords upstream of the cascade. The linear cascade (Figure 1b) contained seven blades based on a low-pressure turbine airfoil geometry that has been studied extensively in the literature,

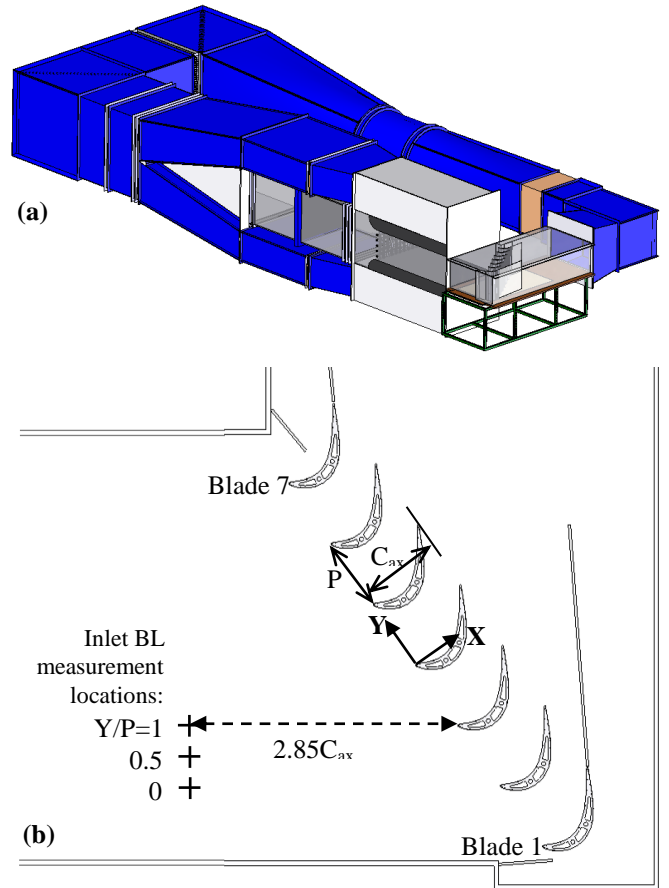


Figure 1. Depiction of (a) the low-speed wind tunnel with corner test section, and (b) the test section with inlet boundary layer measurement locations indicated.

Table 1. Cascade Geometry and Operating Parameters

Scale	8.6X
Axial chord ( $C_{ax}$ )	0.218 m
Span/axial chord ( $S/C_{ax}$ )	2.50
Pitch/axial chord ( $P/C_{ax}$ )	0.826
Inlet angle ( $\beta_{in}$ , relative to axial direction)	$35^\circ$
Exit angle ( $\beta_{exit}$ , relative to axial direction)	$60^\circ$
Zwiefel load coefficient	1.13
Inlet Reynolds number ( $Re_{in} = U_{in} C_{ax} / \nu$ )	$1.25 \times 10^5$
Exit Reynolds number ( $Re_{ex} = U_{exit} C_{ax} / \nu$ )	$2.00 \times 10^5$
Exit Mach number	0.04

particularly with regards to non-axisymmetric endwall contouring (Praisner, et al. [14], Knezevici, et al. [15], Lynch, et al. [18], Lynch, et al. [19]). Table 1 lists the geometrical parameters and operating conditions for the cascade. The cascade was scaled to 8.6 times engine scale and was operated at a Reynolds number matched to the engine condition.

The inlet boundary layer was measured at a location  $2.85C_{ax}$  upstream of the cascade along the inlet flow direction, as indicated in Figure 1b. A 2-component LDV was used to measure streamwise and wall-normal velocities, with velocity bias correction by residence time weighting. Table 2 compares the various boundary layer parameters for stations located upstream of a blade leading edge ( $Y/P=0, 1$ ) and between blade leading edges ( $Y/P=0.5$ ). The boundary layer parameters agreed well and confirmed uniformity of the flow entering the cascade. The results also agreed fairly well with the measurements reported by Lynch, et al. [18].

The top endwall and a side wall of the cascade were constructed of glass for optical access with a laser Doppler velocimeter (LDV). The bottom endwall of the cascade, where measurements were made, was painted flat black and sanded smooth to create a low-reflectivity and hydrodynamically smooth surface. Two types of endwalls were tested in the cascade: a baseline flat endwall, and a three-dimensional non-

axisymmetric contoured endwall. Figure 2a shows an isometric depiction of the non-axisymmetric endwall. The non-axisymmetric contour was designed by the methodology described by Praisner, et al. [14]. The contour shape contained an elevation near the pressure side leading edge of the airfoil, and a depression near the suction side leading edge, as well as an elevated ridge from the pressure to suction side through the passage. The contouring was contained between the inlet and exit planes of the cascade and merged smoothly to the flat endwall level outside of the blade passage.

### Measurement Locations and Coordinate Systems

Flowfield measurements were obtained in an axial plane in the cascade to document the global flowfield, as shown in Figure 2b. The plane was located  $0.2C_{ax}$  downstream of the leading edge plane of the cascade, and is denoted as Plane A. The local coordinate system ( $x, y, z$ ) was aligned to the cascade coordinate system ( $X, Y, Z$ ), although the  $y$ -coordinate origin was shifted so that  $y/P=0$  corresponded to the pressure side of the blade. The  $z$ -coordinate origin was fixed to the flat endwall level, such that regions of the contoured endwall which were below the flat endwall level had negative  $z$ -coordinate values.

Mean velocities were transformed from components aligned with the cascade coordinate system into streamwise and secondary velocity components aligned with the midspan (inviscid) flow direction. The midspan flow direction was determined at each pitchwise location in the measurement plane by:

$$\beta_{ms} = \tan^{-1} \left( \frac{V_{ms}}{U_{ms}} \right) \quad (1)$$

The transformation from local velocities to secondary flow velocities was:

**Table 2. Inlet Boundary Layer at  $2.85C_{ax}$  Upstream**

Variable	Y/P=0	Y/P=0.5	Y/P=1.0	Lynch, et al. [16] (Y/P=1.0)
$\delta_{99}/S$	0.065	0.068	0.076	0.061
$\theta/S$	0.0049	0.0050	0.0051	0.0046
$Re_{\theta}$	1500	1550	1540	1340
H	1.32	1.32	1.30	1.26
Tu	5.9%	5.7%	5.8%	5.9%
$C_f/2$	0.00229	0.00229	0.00231	0.00231

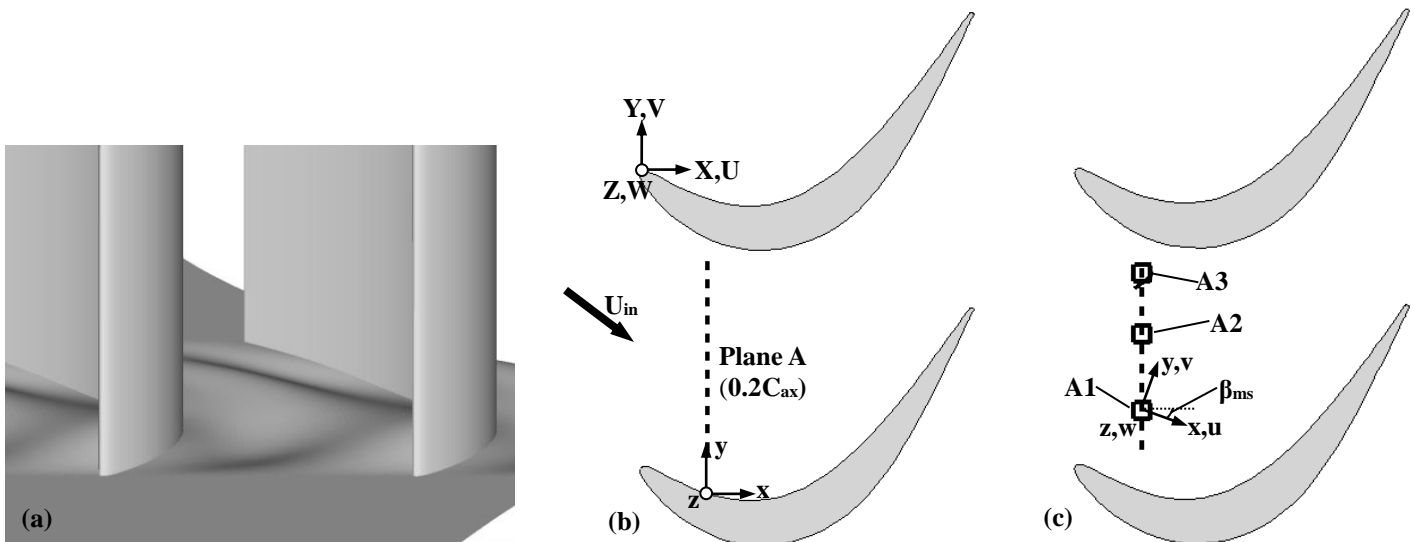


**Figure 2. (a) Isometric view of the contoured endwall; (b) flowfield measurement plane with local coordinate system indicated; and (c) passage boundary layer measurement locations with local velocity transformations indicated.**

$$V_s = U \cos(\beta_{ms}) + V \sin(\beta_{ms}) \quad (2)$$

$$V_n = -U \sin(\beta_{ms}) + V \cos(\beta_{ms}) \quad (3)$$

$$V_z = W \quad (4)$$

Secondary flow vectors are plotted using the normal ( $V_n$ ) and spanwise ( $V_z$ ) components.

Endwall boundary layer profiles were obtained in Plane A at three locations indicated in Figure 2c, and the coordinates of the profile locations are shown in Table 3. The boundary layer measurements in the cascade coordinate system were rotated around the spanwise ( $z$ ) axis into a coordinate system aligned with the freestream velocity direction at the measurement location (same as for the measurement planes). In the rotated coordinate system,  $x$  (and  $u$ ) is the streamwise direction,  $y$  (and  $v$ ) is the cross-stream direction, and  $z$  (and  $w$ ) is the wall-normal (spanwise) direction. It is important to note that for the boundary layer results the origin of the  $z$ -axis was defined relative to the wall at the measurement location.

### Flowfield Measurements

Three-component flowfield measurements were obtained on the bottom endwall of the cascade with a laser Doppler velocimeter (LDV). Green (514.5 nm), blue (488.0 nm), and violet (476.5 nm) beam pairs, with one of each pair frequency-shifted by 40 MHz to resolve directional ambiguity, were transmitted to a two-component probe (green, blue wavelengths) and a single-component probe (violet wavelength). Each probe had a 750 mm focusing lens with a 2.6X beam expander, resulting in a half-angle of  $4.92^\circ$  between beam pairs and fringe spacings of 3.00  $\mu\text{m}$ , 2.84  $\mu\text{m}$ , and 2.78  $\mu\text{m}$  for the green, blue, and violet wavelengths, respectively.

For this study, the two probes were operated in sidescatter mode, where the receiving optics of one probe were used to collect the scattered light from the opposing probe. The measurement volume size had an estimated diameter  $D=72.8 \mu\text{m}$  and a length  $L=200 \mu\text{m}$ . For location A3 with the largest measured shear, the dimensions normalized by inner scaling parameters were  $D^+=3$  and  $L^+=8$ . Atomized di-ethyl-hexyl sebacate, with a diameter of approximately 1  $\mu\text{m}$ , was used as the light-scattering particles. The particles were introduced upstream of the wind tunnel fan, so that they were fully mixed into the flow at the test section. Scattered light collected by the receiving optics was sent to photomultiplier tubes and the resulting signal was processed with an 8-bit digital signal processor.

Three-component coincident measurements were obtained by intersecting the measurement volumes of the green, blue, and

**Table 3. Passage Boundary Layer Locations (Figure 2c)**

Name	Cascade Coordinates		Local Coordinates
	X/C <sub>ax</sub>	Y/P	y/P
A1	0.2	0.19	0.28
A2	0.2	0.44	0.54
A3	0.2	0.65	0.74

violet beam pairs. Several non-orthogonal configurations were used for the flowfield measurements. To obtain measurements in the blade passage, the two probes were suspended above the top endwall and the beams passed through it. The total angle between probes was approximately  $31^\circ$  to  $35^\circ$ , depending on the optical access available at a particular location. For locations near the blade pressure side, the probes were also tilted by  $7^\circ$  (larger than the half-angle of the beam pairs) to minimize interference with the airfoil. The various non-orthogonal configurations and the velocity transformations to cascade coordinates are described in detail in Lynch [20].

The location of the wall was determined through two methods. The output signal from the photodetectors was monitored as the probe volume was moved to the wall. Also, the input power to the LDV was lowered and the beam crossing was visually monitored. Both methods produced nearly identical results and repeatability tests indicated an uncertainty in wall position of less than  $\pm 100 \mu\text{m}$  ( $z^+ \sim 4$  for highest measured shear at location A3).

At each measurement location, 20,000 coincident samples were obtained. Sampling rates ranged from approximately 50 samples/s near the wall to 200 samples/s in the freestream. Instantaneous velocity measurements were accepted when burst signals from each channel overlapped by less than 200% of their burst signal elapsed times. This essentially resulted in an adaptive coincidence window that became more restrictive for higher-velocity measurements, since the transit time of a particle is inversely related to its velocity. For low-velocity measurements (i.e., long burst times), the adaptive coincidence window method produced identical results to a fixed coincidence window of 10  $\mu\text{s}$ . Measurements in non-orthogonal coordinates were transformed to the orthogonal blade cascade coordinates, and further transformed depending on the local coordinate system. Velocity bias correction was performed by using the inverse of the instantaneous velocity magnitude as a weighting factor.

A sequential perturbation analysis (Moffat [21]) was used to estimate uncertainty of the LDV measurements, which included the effect of measurement bias and angular uncertainty in the probe orientation on the transformed velocity components. Uncertainty in the probe orientation angles in the non-orthogonal setup was estimated to be  $\pm 0.5^\circ$ , and the measurement bias was estimated as  $\pm 1\%$  of the measured value. Precision uncertainties were estimated at a 95% confidence interval, and the root-sum-square of bias and precision uncertainties gave the total uncertainty. Table 4 lists the estimated total uncertainties for measurements obtained in a highly turbulent region ( $y/P=0.28$ ,  $z/S=0.015$ ) at station A3 in Plane A (see Figure 2b). Note that quantities involving the spanwise component of velocity ( $w$ ) have higher uncertainty than the other velocity components since that component was the most sensitive to the angle between probes in the non-orthogonal configuration.

### Wall Shear Stress Measurements

Endwall shear stress measurements were obtained using an oil film interferometry (OFI) technique, in which the shear rate of an oil film is directly related to the shear stress acting on it. Naughton and Sheplak [22] provide a thorough review of the technique. Implementation on turbine cascade endwalls was described by Harrison [8], Holley, et al. [23], and Holley and Langston [24]. The method used in this study was described in detail by Lynch and Thole [25], and only a short treatment is given here.

The time-averaged shear rate of the oil can be determined by measuring the change in height (thickness) of the film over a discrete time interval, with an order-of-magnitude analysis indicating that shear is the dominant force by at least an order of magnitude. The average shear rate multiplied by the oil viscosity gives the average shear stress acting on the surface of the film. In this implementation, only the final height of the oil film was required since the conditions leading to it were integrated over the tunnel run time. The height of the oil film is

**Table 4. Estimated Uncertainties at a Highly Turbulent Location in Plane A**

Variable	Mean	Uncertainty	% of Mean
$u/U_{in}$	0.436	$\pm 0.011$	$\pm 2.6\%$
$v/U_{in}$	0.207	$\pm 0.0065$	$\pm 3.1\%$
$w/U_{in}$	-0.030	$\pm 0.0053$	$\pm 17.5\%$
$\beta$	$25.4^\circ$	$\pm 0.5^\circ$	$\pm 2.0\%$
$V_s/U_{in}$	0.390	$\pm 0.041$	$\pm 1.3\%$
$V_n/U_{in}$	0.283	$\pm 0.036$	$\pm 1.6\%$
$V_z/U_{in}$	-0.030	$\pm 0.0053$	$\pm 17.5\%$
$k/U_{in}^2$	0.023	$\pm 0.0011$	$\pm 4.9\%$
$\bar{u}'/U_{in}$	0.143	$\pm 0.0037$	$\pm 2.6\%$
$\bar{v}'/U_{in}$	0.130	$\pm 0.0034$	$\pm 2.6\%$
$\bar{w}'/U_{in}$	0.089	$\pm 0.0028$	$\pm 3.2\%$
$C_f/2$	0.00439	$\pm 3.51e-4$	$\pm 8\%$
$\beta_w - \beta_{ms}$	$64^\circ$	$\pm 4^\circ$	$\pm 6\%$

measured using interferometry, whereby illumination of the film by a monochromatic light source produces constructive and destructive interference bands. Figure 3a depicts the development of the interferogram bands in an oil film, and Figure 3b shows a sample interferogram. The direction of the limiting streamline (endwall shear direction) was determined by the direction of small streaks in the oil film at the measurement point; see Figure 3b.

For implementation in the cascade, silicone oil droplets were applied to nickel foil patches adhered to the endwall surface. The nickel foil was 50  $\mu\text{m}$  thick and the final thickness of the oil film was less than 1  $\mu\text{m}$ ; thus, the total thickness of the foil patch and oil film was not expected to disturb the flow ( $z^+ < 2$  for the highest shear measured). A typical run length to obtain measurable interferograms was approximately twenty minutes, with start-up and shutdown transients being less than 45 seconds of that time. The foil patches were carefully removed after a test and immediately imaged in a fixture with a nearly monochromatic sodium vapor lamp ( $\lambda = 589, 589.6 \text{ nm}$ ) to obtain the interferograms. Measurements were repeated several times with different oil viscosities, foil patch positions, and oil droplet placement techniques. Results were within experimental uncertainty for the technique.

Benchmarking was performed for this study by comparing endwall shear stress obtained with OFI to the shear values derived from a fit to the log-law region of the two-dimensional boundary layer measured upstream of the cascade. OFI measurements were within 6% of the boundary layer-derived shear values at locations  $5.4C_{ax}$  ( $Re_0 = 1060$ ),  $3.0C_{ax}$  ( $Re_0 = 1510$ ), and  $0.75C_{ax}$  ( $Re_0 = 2090$ ) upstream of the blade cascade.

The partial derivative method described by Moffat [21] was used to calculate uncertainties for the measurements of friction coefficient magnitude and direction. Table 4 lists the friction coefficient uncertainty at station A3. Directional uncertainty was estimated as  $\partial\beta_w = \pm 4^\circ$ . Magnitude uncertainty (including the effect of the limiting streamline direction uncertainty) was estimated as  $\partial C_f = \pm 8\%$  and was dominated by uncertainty in the interferogram spacing.

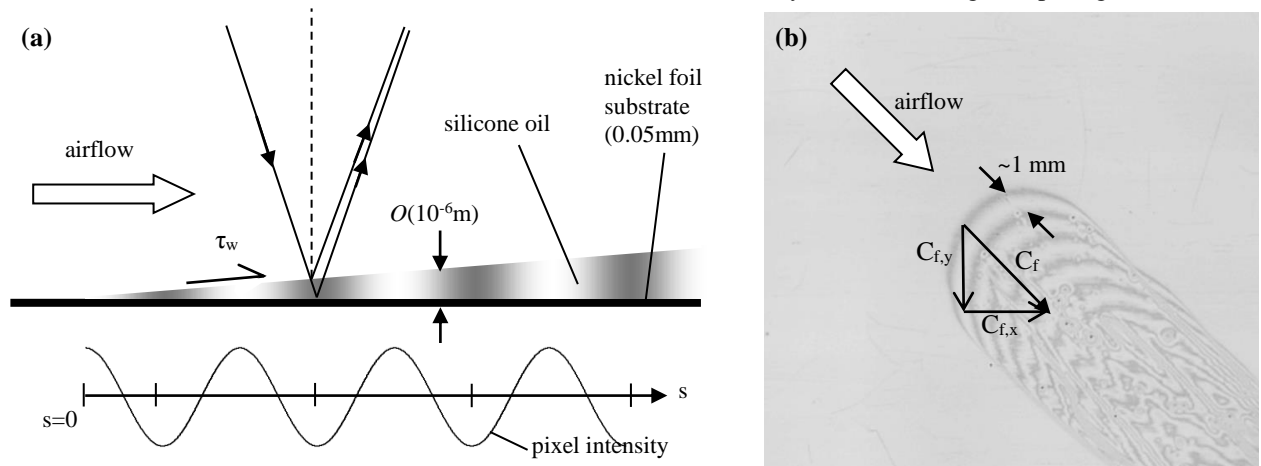


**Figure 3. (a) Schematic of oil film development due to shear, and (b) sample interferogram which demonstrates friction coefficient directionality.**

## RESULTS

The results presented in this paper include flowfield measurements at a plane within the cascade, as well as three-component boundary layer profiles at three locations in the plane. The flow measurements are compared to friction coefficients and previously measured endwall heat transfer coefficients reported by Lynch, et al. [18]. A check of the flowfield measurements was performed by comparing the streamwise mean velocity and flow angle to a benchmarked prediction of the cascade flow by Lynch, et al. [19]. Figure 4a-b compare the measured streamwise velocity and flow angle at midspan to the prediction. Refer to Figure 2b for the definition of  $y/P$  for Plane A. Streamwise velocity in Figure 4a varies significantly across the passage. Mean flow angles in Figure 4b indicate that the variation of turning within the plane is less than  $10^\circ$ . LDV measurements and predictions also show good agreement for the mean flow angle.

Endwall oil flow patterns presented by Lynch, et al. [18] are reproduced in Figure 5a-b for the flat and contoured endwalls. Streaklines were drawn on the oil flow patterns and major secondary flow features associated with the passage and corner vortices were identified. In Figure 5, three-dimensional separation lines associated with the pressure and suction-side legs of the horseshoe vortex, as well as the flowfield measurement planes and boundary layer profile locations, are added. The endwall flow pattern is helpful in interpreting the flowfield results presented next.

## Plane A Flowfield Measurements

Figure 6 shows contours of mean streamwise velocity overlaid with mean secondary velocity vectors at Plane A for the flat and contoured endwalls. The gray areas indicate the locations of the endwall and adjacent airfoils, with the pressure and suction sides of the passage indicated by PS and SS, respectively. Note that due to limitations of optical access, measurements could not be obtained closer than  $y/P=0.14$  from the pressure side or  $y/P=0.06$  from the suction side. All velocities in Figure 6 are normalized by the inlet freestream velocity. Vertical lines in the figure indicate the locations of the boundary layer profiles presented later.

The flowfield results for the flat endwall (Figure 6a) are discussed first. In the freestream (above  $z/S=0.20$ ), streamwise velocity contours indicate the low-velocity flow near the pressure side, and higher-velocity flow near the suction side due to acceleration around the airfoil. Below  $z/S=0.12$ , streamwise velocity decreases at a given pitchwise location due to the boundary layer at the endwall. Secondary velocity vectors indicate the presence of a distinct vortex near the pressure side, centered around  $y/P=0.26$ ,  $z/S=0.05$ , which brings fluid down to the endwall. Lynch, et al. [18] indicated high levels of endwall heat transfer near the pressure side for the flat endwall. Secondary vectors near the suction side indicate upward movement of fluid that is associated with the separation of the turbulent inlet boundary layer from the endwall.

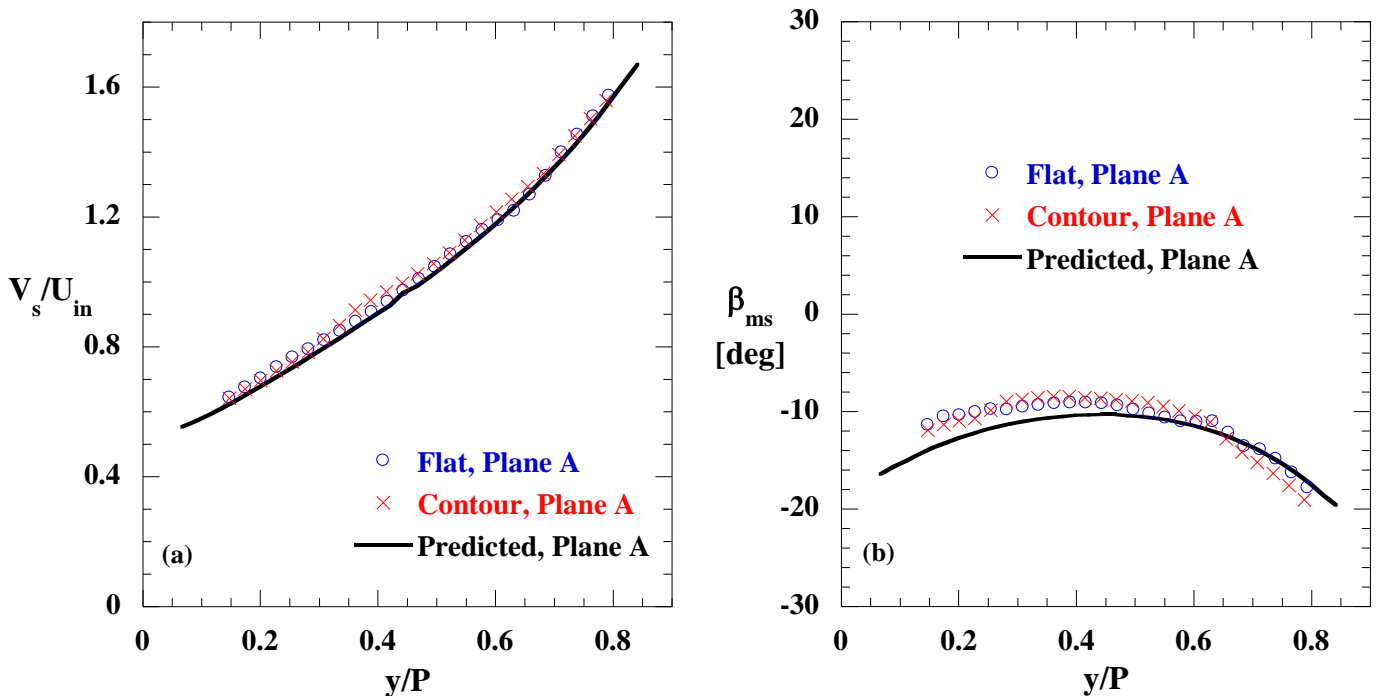


Figure 4. (a) Measurements and predictions of streamwise velocity at midspan for Plane A, and (b) measurements and predictions of flow angles at midspan.

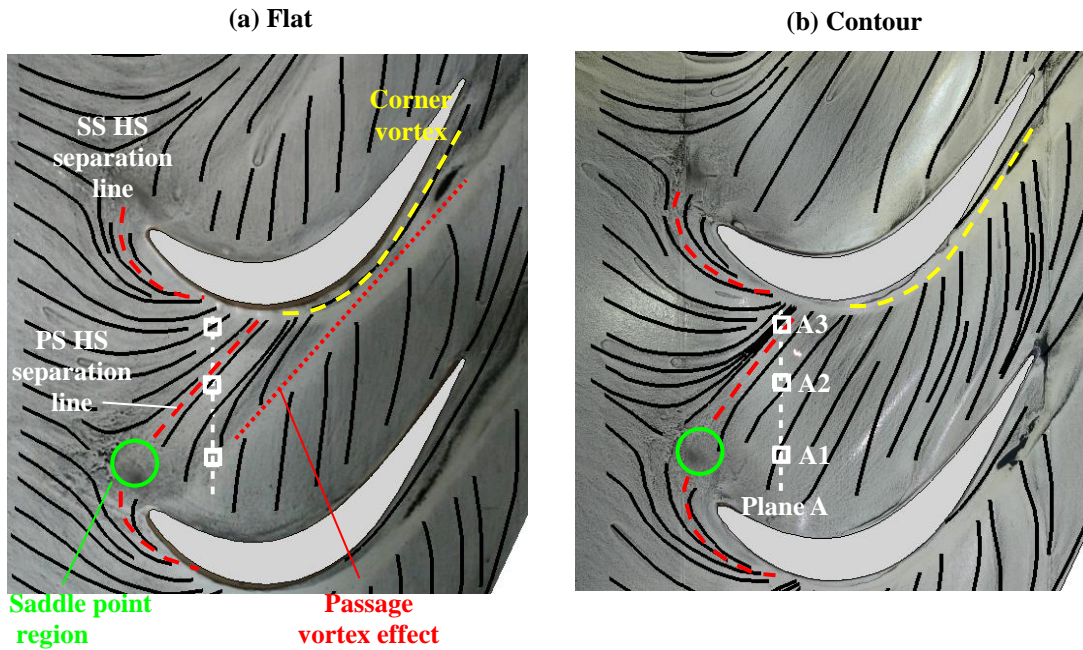


Figure 5. (a) Endwall oil flow visualization of Lynch, et al. [16] for the (a) flat and (b) contoured endwalls, overlaid with the measurement locations in this study.

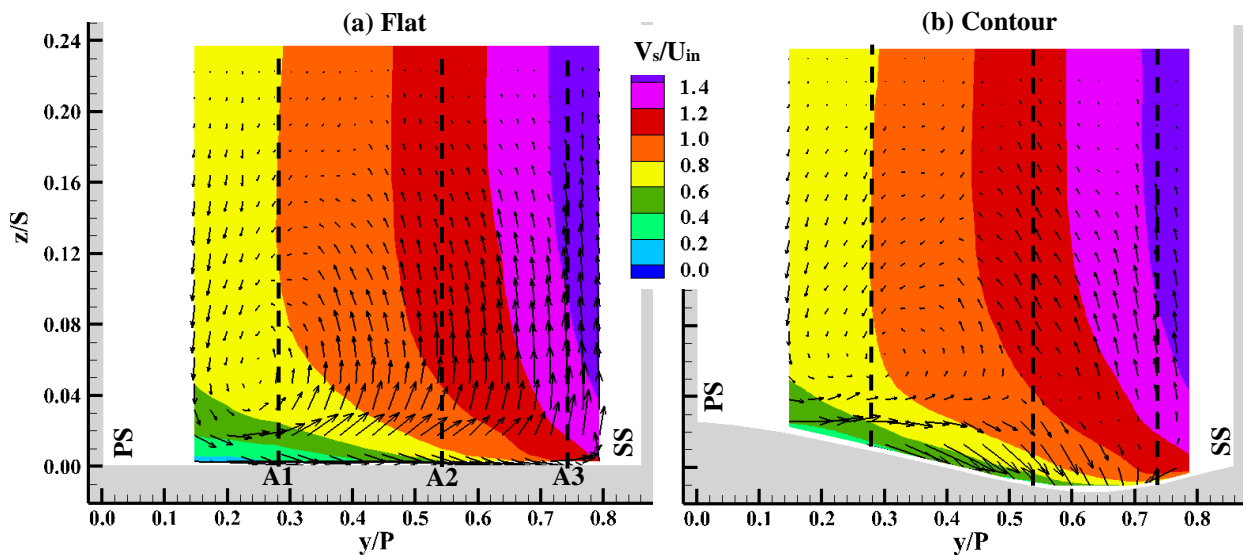


Figure 6. Contours of mean streamwise velocity and mean secondary velocity vectors at Plane A (see Figure 2) for the (a) flat and (b) contoured endwalls.

The contoured endwall has a significant effect on the mean flowfield, as seen by comparing Figure 6a and b. The rise in the contour near the pressure side accelerates the near-wall flow and increases the streamwise velocity, but  $V_s/U_{in}$  contours near the depression indicate lower streamwise velocity compared to the flat endwall. Secondary vectors in Figure 6b indicate a less-distinct vortex displaced further from the pressure side (center at  $y/P=0.3$ ,  $z/S=0.06$ ) than in the flat endwall measurements. The secondary vectors also indicate a significant downward flow toward the middle of the passage, as the near-wall flow follows the wall down into the depression.

Turbulent kinetic energy (TKE) normalized by the inlet freestream velocity is shown in Figure 7. The results for the flat endwall (Figure 7a) indicate high levels of TKE under the large vortex seen in the mean velocity results (Figure 6a). Peak TKE levels correspond to a turbulence intensity of 11% based on the inlet freestream velocity. Kang and Thole [26] found a similar region of high turbulence under a large streamwise vortex located near the pressure side leading edge of a vane. A small circular region of high TKE is also seen near the suction side of the passage, which corresponds to the suction side leg of the horseshoe vortex. In comparison to the flat endwall, the contour (Figure 7b) has slightly higher peak TKE levels near the

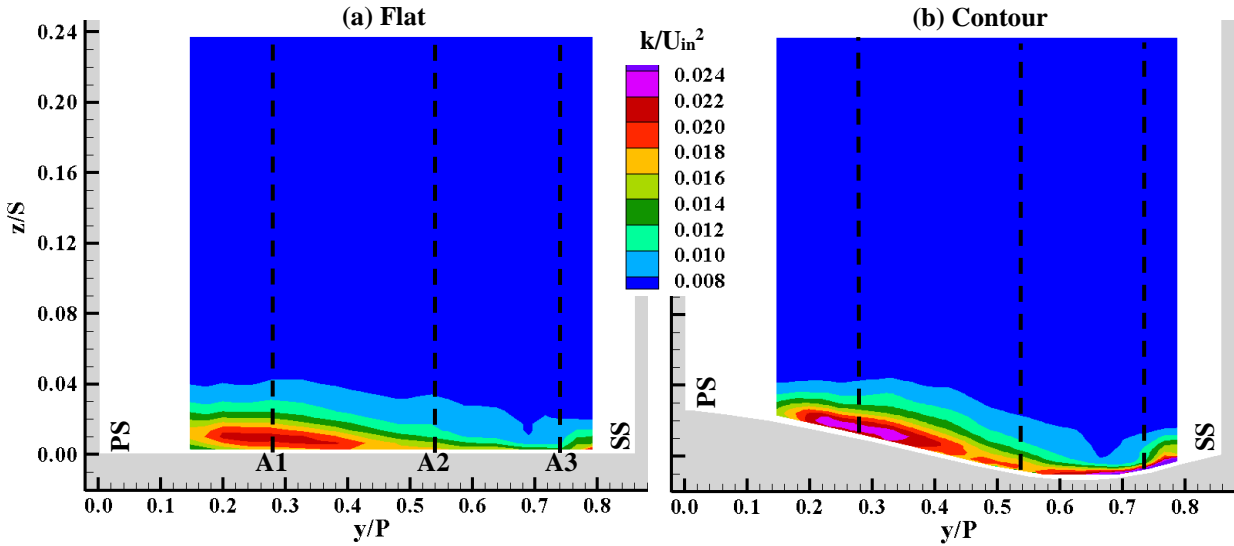


Figure 7. Contours of turbulent kinetic energy normalized by inlet velocity magnitude at Plane A for the (a) flat and (b) contoured endwalls.

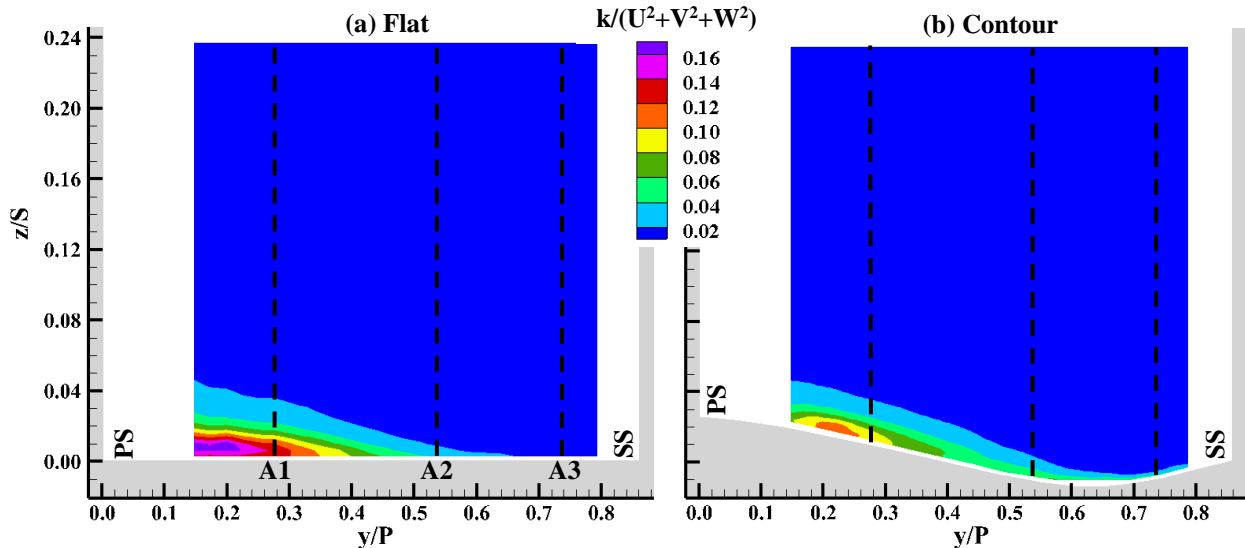


Figure 8. Contours of turbulent kinetic energy normalized by the local velocity magnitude at Plane A for the (a) flat and (b) contoured endwalls.

pressure side, and a larger extent of high TKE levels near the endwall across the passage. TKE associated with the suction side horseshoe vortex is also increased. This might seem like a surprising result since the contour was shown in Figure 6 to reduce mean secondary flow relative to the flat endwall; however, it is an artifact of the TKE normalization method in Figure 7, where choosing the inlet velocity as a normalization value results in a direct comparison of TKE magnitudes. Note from Figure 6 that the local velocity is higher near the pressure side with endwall contouring, and thus it is instructive to look at TKE relative to the local velocity magnitude. This is shown for the flat and contoured endwalls in Figure 8. It is apparent in Figure 8 that the contoured endwall produces a lower relative TKE than the flat endwall around the region of the downwash

associated with the passage vortex. This is connected to the reduced generation of loss by contouring; measurements by Knezevici, et al. [15] at  $0.63C_{ax}$  downstream of the blade leading edge for this same airfoil and contour shape show reduced passage vortex loss with contouring.

### Plane A Boundary Layers

Figure 9 shows endwall boundary layer profiles of streamwise mean velocity at stations A1-A3 in Plane A. Recall that the velocities at each station were transformed into the local inviscid freestream direction per Figure 2c. Also included for reference is the 1/7th power law profile for a turbulent boundary layer, and the Blasius laminar boundary layer profile. Table 5 summarizes the boundary layer parameters for A1-A3.

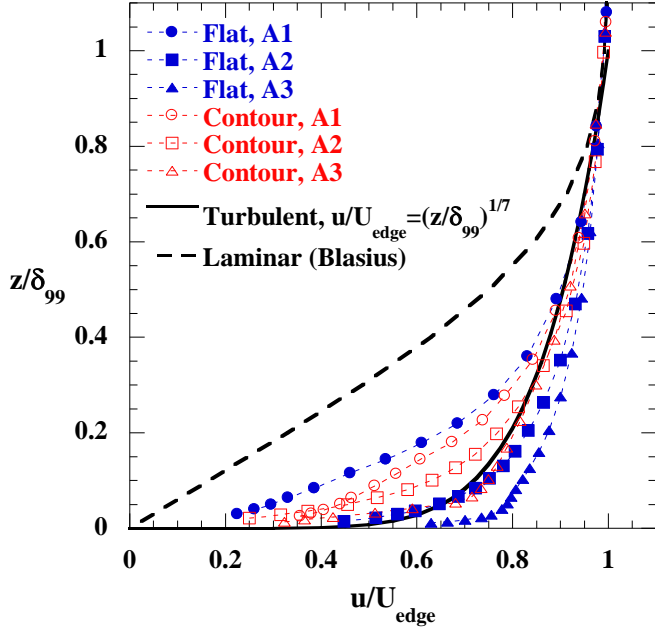


**Figure 9. Boundary layer profiles of mean streamwise velocity in Plane A for the flat and contoured endwalls.**

At station A1, the streamwise velocity profile for the flat endwall falls between the turbulent and laminar zero-pressure-gradient profiles, although the streamwise momentum thickness Reynolds number and shape factor in Table 5 suggest that the flow is turbulent. The oil flow pattern in Figure 5a shows that station A1 is near the development of the passage vortex for the flat endwall. In this case, the laminar-like shape of the streamwise velocity profile at A1 is partially an indication of the amount of crossflow in the boundary layer, where flow is being turned away from the inviscid streamwise direction by the rotation of the passage vortex and thus does not contribute to the streamwise velocity profile. For the contoured endwall, the passage vortex is displaced away from the pressure side, reducing the effect of the passage vortex on the contour streamwise velocity profile at A1. Flow acceleration at the

contour elevation near the pressure side decreases the momentum thickness Reynolds number and shape factor for the contour relative to the flat endwall in Table 5.

At station A2, the flat endwall streamwise profile is relatively close to the 1/7th power law profile, but the contoured endwall profile has lower near-wall velocities. The displaced passage vortex, as well as deceleration of flow entering the contour depression, reduces the near-wall streamwise velocity. In contrast to station A1 results, the contour profile at A2 has a larger momentum thickness Reynolds number and shape factor than the flat endwall.

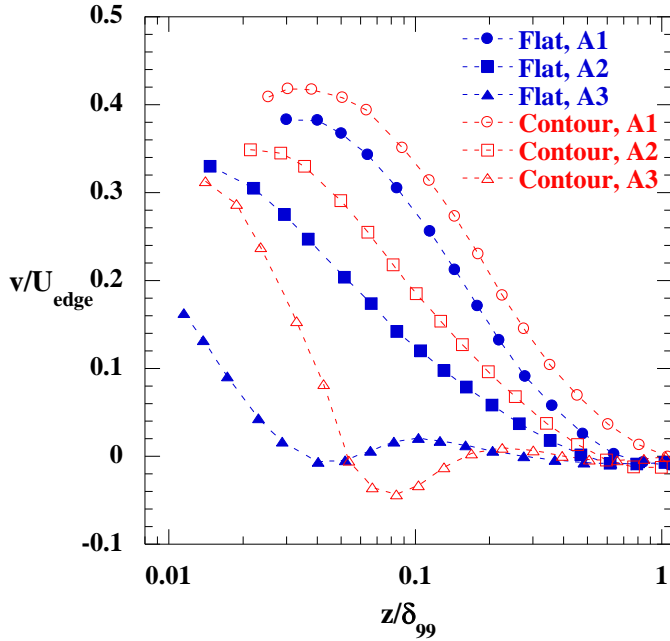
Streamwise velocity profiles at A3 are influenced by the acceleration of endwall flow toward the airfoil suction side, as well as the effect of the suction side horseshoe vortex. In the case of the flat endwall, strong acceleration toward the suction side results in a more full boundary layer at A3. In contrast, the contour reduces the streamwise pressure gradient near the suction side, and the boundary layer profile is less full compared to the flat endwall.

Figure 10 presents the cross-stream velocities at each of the measurement stations in Plane A. Note that the abscissa is plotted on a log scale to emphasize the near-wall region. At station A1, cross-stream velocities are extremely large, peaking at nearly 40% of the boundary layer edge velocity. The contour exhibits higher cross-stream velocity than the flat endwall, due to the acceleration of flow at the contour elevation. At station A2, the contour also has higher cross-stream velocity, but in this case it is due to the displaced passage vortex which turns flow away from the inviscid streamwise direction. The hooked profile at station A3 for the contour is a result of the influence of the suction side leg of the horseshoe vortex displaced away from the suction side of the passage.

The mean flow angle relative to the midspan angle is shown in Figure 11. The data points below  $z/\delta_{99}=0.01$  are the wall shear angles from the OFI measurements, where the spanwise location was estimated using the thickness of the foil patch as the measurement height. Station A1 profiles in Figure 11 show very large skew angles, exceeding  $70^\circ$  for the flat

**Table 5. Plane A Boundary Layer Parameters From Flowfield Measurements**

Name	A1		A2		A3	
	Flat	Contour	Flat	Contour	Flat	Contour
$U_{edge}/U_{in}$	0.79	0.79	1.10	1.11	1.46	1.43
$\delta_{99}/S$	0.091	0.072	0.124	0.128	0.159	0.194
$\theta/S$	0.0100	0.0073	0.0100	0.0120	0.0110	0.0178
$Re_\theta$	2230	1670	3050	3810	4370	7175
H	1.63	1.47	1.32	1.47	1.24	1.36
Tu	6.5%	6.2%	4.3%	4.3%	3.3%	3.3%
$C_f/2$ , OFI	0.00337	0.00439	0.00310	0.00228	0.00277	0.00251
$C_f/2$ , Clauser fit to velocity magnitude	0.00143	0.00201	0.00187	0.00140	0.00211	0.00137
$\beta_{ms}$	$-10.4^\circ$	$-10.6^\circ$	$-10.5^\circ$	$-9.9^\circ$	$-14.9^\circ$	$-17.0^\circ$
$\beta_w$	$62^\circ$	$53^\circ$	$43^\circ$	$54^\circ$	$29^\circ$	$48^\circ$



**Figure 10. Boundary layer profiles of mean cross-stream velocity in Plane A for the flat and contoured endwalls.**

endwall. Due to the displacement and weakening of the passage vortex with endwall contouring, flow angle deviation is reduced at A1 but increased at A2 relative to the flat endwall. The profiles at station A3 indicate the effect of the suction side leg of the horseshoe vortex.

Endwall heat transfer ( $St$ ) and friction coefficients ( $C_f$ ) at Plane A are shown in Figure 12. The heat transfer coefficients are shown as continuous lines, since they were extracted from spatially-resolved measurements obtained by Lynch, et al. [18]. For those measurements, surface temperatures were measured by an infrared camera on a constant heat flux surface covering the entire endwall (see Lynch, et al. [18] for details). Friction coefficients were obtained only at stations A1-A3. The velocity scale for  $St$  and  $C_f$  is the local freestream velocity. Recall from Figure 6a that the inviscid streamwise velocity magnitude is lower near the pressure side than the suction side, which accentuates differences in  $St$  (or  $C_f$ ) across the passage. Heat transfer coefficient levels for the flat endwall are high toward the pressure side of the passage ( $y/P=0$ ), where the downward-turning fluid impinges on the endwall. Around  $y/P=0.7$ ,  $St$  values are low where the turbulent boundary layer is skewed but not separated from the endwall. The heat transfer coefficient increases slightly near the suction side due to the downwash and increased turbulence of the suction side horseshoe vortex.

The flat endwall friction coefficient agrees reasonably well with the  $St$  number at station A1. At this location under the passage vortex, the flow is generally parallel to the wall and turbulent transport mechanisms of momentum and heat transfer are similar, despite the significant three-dimensionality of the boundary layer. At station A2, however, the flat endwall friction coefficient is higher than the heat transfer coefficient. Although

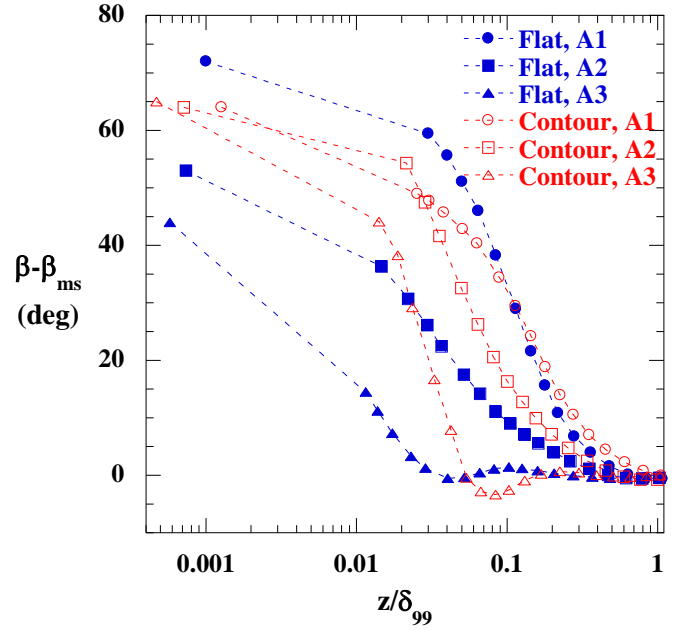


**Figure 11. Boundary layer profiles of mean flow angle relative to the freestream angle in Plane A, for the flat and contoured endwalls. The results below  $z/\delta=0.01$  are wall shear angles from the friction coefficient measurements.**

part of the variation between  $St$  and  $C_f$  can be attributed to the cross-passage favorable pressure gradient, the oil flow visualization in Figure 5a indicates that A2 is slightly downstream of the pressure side horseshoe vortex separation line, which is associated with the pressure side leg of the horseshoe vortex. Holley and Langston [24] also indicate that friction coefficients around the separation line are higher on the downstream side where the vortex sweeps flow to the endwall. The friction coefficient for station A3 is higher than the endwall heat transfer coefficient due to the strong favorable pressure gradient accelerating the flow close to the suction side.

Contoured endwall heat transfer in Figure 12 is high near the pressure side and low around  $y/P=0.7$ , with levels similar to the flat endwall in those areas. From approximately  $0.2 < y/P < 0.55$ , however, the contour results in higher  $St$  values relative to the flat endwall. Comparison to the flowfield measurements suggests that the area of high streamwise velocity (Figure 6) and near-wall turbulent kinetic energy (Figure 7) between  $0.2 < y/P < 0.55$  corresponds well to the increased heat transfer for the contour at this location.

The contoured endwall friction coefficient in Figure 12 agrees well with  $St$  at station A1, and demonstrates an increase in  $C_f$  for the contour versus the flat endwall. The percent increase in  $C_f$  at station A1 is 23%, which compares well with the percent increase of 24% in  $St$ . At station A2, however,  $C_f$  and  $St$  have nearly the same magnitude for the contoured endwall, unlike the situation for the flat endwall. Figure 5b indicates that the separation line has been displaced upstream with contouring, and thus the pressure side horseshoe vortex

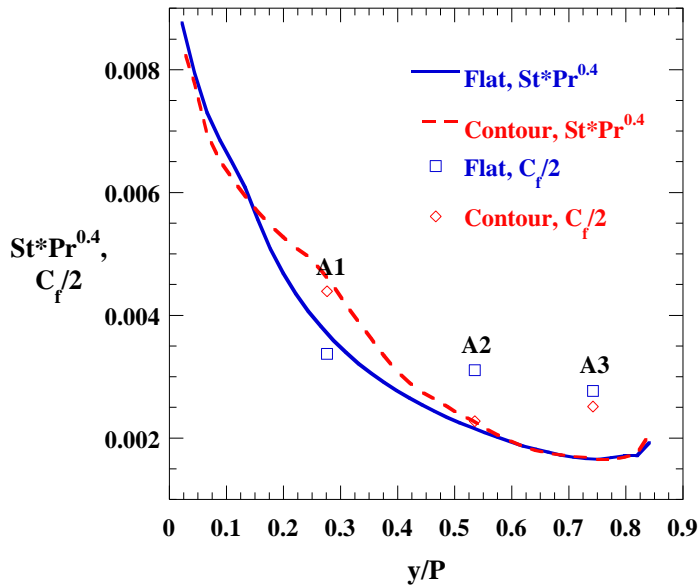


**Figure 12. Measured endwall heat transfer and friction coefficients at Plane A, where the velocity scale for  $St$  and  $C_f$  is the local freestream velocity.**

would be expected to have less of an influence on the wall shear at A2.

At station A3, the friction coefficient is higher than the corresponding Stanton number for the contoured endwall. The level of  $C_f$  is the same between the flat and contoured endwalls at this location. Although the magnitudes of  $C_f$  and  $St$  are different at station A3, both parameters indicate no significant difference between the flat and contoured endwalls. Strong flow acceleration close to the suction side has a significant role in minimizing differences between the two endwall geometries.

## CONCLUSIONS

Mean and fluctuating velocity measurements obtained with a three-component laser Doppler velocimeter were presented for a turbine cascade with and without non-axisymmetric endwall contouring. The three-dimensional flowfield was measured at a plane within the cascade. Boundary layer profiles were also obtained at three locations in the passage to understand the effect of the contour on the highly skewed endwall boundary layer. Friction coefficients at the selected boundary layer locations were measured with the oil film interferometry technique and compared to previously measured heat transfer coefficients.

Flowfield measurements in the passage indicated low streamwise velocity and high turbulent kinetic energy near the pressure side associated with secondary flow circulation of the passage vortex. When compared to a flat endwall, the contour resulted in increased streamwise velocity, reduced secondary flow velocities, and reduced turbulent kinetic energy (when normalized by local velocity magnitude). A region of elevated endwall heat transfer seen in previously obtained results for the contour correlated well with the region of elevated turbulent

kinetic energy. Boundary layer profiles indicated skew angles greater than  $70^\circ$  between the endwall and freestream for the flat endwall near the pressure side, reflecting the influence of the passage vortex. Near the suction side of the passage, the contoured endwall caused displacement of the suction side horseshoe vortex away from the airfoil-endwall corner and increased turbulent kinetic energy associated with the vortex, compared to the flat endwall.

Overall, non-axisymmetric contouring displaced the passage vortex and reduced its relative unsteadiness. The shift of the vortex caused that feature to increase local heat transfer levels relative to the flat endwall near the pressure side. However, the resulting smaller passage vortex with contouring had a reduced influence on the endwall boundary layer and thus would be expected to have lower overall impact to the endwall heat transfer.

## ACKNOWLEDGMENTS

The authors gratefully acknowledge United Technologies—Pratt & Whitney for their support of this work, particularly Atul Kohli and Christopher Lehane for their advice and technical input, and Eunice Bradley-Allen for performing the endwall contour design. We would also like to thank Brian Holley and Lee Langston for providing the raw materials for the OFI method.

## REFERENCES

- [1] Langston, L. S., Nice, M. L., and Hooper, R. M., 1977, "Three-Dimensional Flow within a Turbine Cascade Passage," *J. Eng. Power*, 99, pp. 21-28.
- [2] Sharma, O. P., and Butler, T. L., 1987, "Predictions of Endwall Losses and Secondary Flows in Axial Flow Turbine Cascades," *J. Turbomach.*, 109(2), pp. 229-236.
- [3] Sieverding, C. H., 1985, "Recent Progress in the Understanding of Basic Aspects of Secondary Flows in Turbine Blade Passages," *J. Eng. Gas Turbines Power*, 107(2), pp. 248-257.
- [4] Anderson, S. D., and Eaton, J. K., 1989, "Reynolds Stress Development in Pressure-Driven Three-Dimensional Turbulent Boundary Layers," *J. Fluid Mech.*, 202, pp. 263-294.
- [5] Johnston, J. P., and Flack, K. A., 1996, "Review---Advances in Three-Dimensional Turbulent Boundary Layers with Emphasis on the Wall-Layer Regions," *J. Fluids Engr.*, 118(2), pp. 219-232.
- [6] Lewis, D. J., and Simpson, R. L., 1998, "Turbulence Structure of Heat Transfer through a Three-Dimensional Turbulent Boundary Layer," *J. Thermophys. Heat Transfer*, 12(2), pp. 248-255.
- [7] Shizawa, T., and Eaton, J. K., 1992, "Turbulence Measurements for a Longitudinal Vortex Interacting with a Three-Dimensional Turbulent Boundary Layer," *AIAA J.*, 30(1), pp. 49-55.
- [8] Harrison, S., 1990, "Secondary Loss Generation in a Linear Cascade of High-Turning Turbine Blades," *J. Turbomach.*, 112(4), pp. 618-624.

- [9] Vera, M., Blanco, E. d. I. R., Hodson, H., and Vazquez, R., 2009, "Endwall Boundary Layer Development in an Engine Representative Four-Stage Low Pressure Turbine Rig," *J. Turbomach.*, 131(1), p. 011017.
- [10] Harvey, N. W., Rose, M. G., Taylor, M. D., Shahpar, S., Hartland, J., and Gregory-Smith, D. G., 2000, "Nonaxisymmetric Turbine End Wall Design: Part I--- Three-Dimensional Linear Design System," *J. Turbomach.*, 122(2), pp. 278-285.
- [11] Hartland, J. C., Gregory-Smith, D. G., Harvey, N. W., and Rose, M. G., 2000, "Nonaxisymmetric Turbine End Wall Design: Part II---Experimental Validation," *J. Turbomach.*, 122(2), pp. 286-293.
- [12] Germain, T., Nagel, M., Raab, I., Schupbach, P., Abhari, R. S., and Rose, M., 2010, "Improving Efficiency of a High Work Turbine Using Nonaxisymmetric Endwalls--- Part I: Endwall Design and Performance," *J. Turbomach.*, 132(2), p. 021007.
- [13] Schuepbach, P., Abhari, R. S., Rose, M. G., Germain, T., Raab, I., and Gier, J., 2010, "Improving Efficiency of a High Work Turbine Using Nonaxisymmetric Endwalls---Part II: Time-Resolved Flow Physics," *J. Turbomach.*, 132(2), p. 021008.
- [14] Praisner, T. J., Allen-Bradley, E., Grover, E. A., Knezevici, D. C., and Sjolander, S. A., "Application of Non-Axisymmetric Endwall Contouring to Conventional and High-Lift Turbine Airfoils," Proc. ASME Turbo Expo 2007, GT2007-27579.
- [15] Knezevici, D. C., Sjolander, S. A., Praisner, T. J., Allen-Bradley, E., and Grover, E. A., 2010, "Measurements of Secondary Losses in a Turbine Cascade with the Implementation of Nonaxisymmetric Endwall Contouring," *J. Turbomach.*, 132(1), p. 011013.
- [16] Saha, A. K., and Acharya, S., 2008, "Computations of Turbulent Flow and Heat Transfer through a Three-Dimensional Nonaxisymmetric Blade Passage," *J. Turbomach.*, 130(3), p. 031008.
- [17] Panchal, K. V., Abraham, S., Ekkad, S., Ng, W. F., Lohaus, A. S., and Crawford, M. E., "Effect of Endwall Contouring on a Transonic Turbine Blade Passage: Part 2--Heat Transfer Performance," Proc. ASME Turbo Expo 2012, GT2012-68405.
- [18] Lynch, S. P., Sundaram, N., Thole, K. A., Kohli, A., and Lehane, C., 2011, "Heat Transfer for a Turbine Blade with Nonaxisymmetric Endwall Contouring," *J. Turbomach.*, 133(1), pp. 011019-011019.
- [19] Lynch, S. P., Thole, K. A., Kohli, A., and Lehane, C., 2011, "Computational Predictions of Heat Transfer and Film-Cooling for a Turbine Blade with Nonaxisymmetric Endwall Contouring," *J. Turbomach.*, 133(4), pp. 041003-041010.
- [20] Lynch, S. P., 2011, "The Effect of Endwall Contouring on Boundary Layer Development in a Turbine Blade Passage," PhD, Virginia Tech.
- [21] Moffat, R. J., 1988, "Describing the Uncertainties in Experimental Results," *Exp. Therm Fluid Sci.*, 1, pp. 3-17.
- [22] Naughton, J. W., and Sheplak, M., 2002, "Modern Developments in Shear-Stress Measurement," *Prog. Aerosp. Sci.*, 38(6-7), pp. 515-570.
- [23] Holley, B. M., Bezz, S., and Langston, L. S., 2006, "Measurement and Calculation of Turbine Cascade Endwall Pressure and Shear Stress," *J. Turbomach.*, 128(2), pp. 232-239.
- [24] Holley, B. M., and Langston, L. S., 2009, "Surface Shear Stress and Pressure Measurements in a Turbine Cascade," *J. Turbomach.*, 131(3), pp. 031014-031018.
- [25] Lynch, S. P., and Thole, K. A., 2008, "The Effect of Combustor-Turbine Interface Gap Leakage on the Endwall Heat Transfer for a Nozzle Guide Vane," *J. Turbomach.*, 130(4), p. 041019.
- [26] Kang, M. B., and Thole, K. A., 2000, "Flowfield Measurements in the Endwall Region of a Stator Vane," *J. Turbomach.*, 122(3), pp. 458-466.